Effects of Ag NPs: Enhancement of Mechanical Properties of Er^3+/Nd^3+ Codoped Lithium Niobate Tellurite Glass via Ultrasonic Measurement

Effects of Ag NPs: Enhancement of Mechanical Properties of Er^{3+}/Nd^{3+} Codoped Lithium Niobate Tellurite Glass via Ultrasonic Measurement

Nurhafizah H.[a*], Nurulwahidah Z.A.S. [a], Anis Nazihah M.D. [b], Nur Hidayah A.[a]

[a] Advanced Optical Materials Research Group, Faculty of Science, Universiti Teknologi Malaysia, 81310 UTM Johor Bahru, Johor, Malaysia.

[b]Faculty of Sciences and Mathematics, Kampus Sultan Azlan Shah (KSAS), Universiti Pendidikan Sultan Idris (UPSI), Proton City, 35900 Tanjung Malim, Perak, Malaysia.

E-mail: nurhafizah.h@utm.my

Abstract. Ag NPs embedded in Er^{3+}/Nd^{3+} codoped lithium niobate tellurite glasses of the form (68-x)TeO_2-15Li_2CO_3-15Nb_2O_5-1Er_2O_3-1Nd_2O_3-(x)AgCl with x = 1, 2 and 3 mol% via conventional melt-quenching technique. Surface roughness and mechanical properties of the glass sample are characterized and discussed. The ultrasonic attenuation shows the rate of sound energy reduction when an ultrasonic wave is propagating in a medium which is the lithium niobate tellurite glasses. The glass attenuation depends on the grain size, viscous friction, crystal structure, porosity, and hardness. The ultrasonic acoustic impedance and attenuation coefficient of particles are estimated from an analysis of the pulse-echo technique. Simple correlation functions and the accurate scattering theory include the effects of acoustic waves, were used separately to focus on the absorption and scattering effects from spherical particles (Ag NPs) and thereby describe the structures of the medium.

1. Introduction

Lately, optical behavior of rare-earth (RE) doped silicate, phosphate, borate and tellurite based glasses have been studied thoroughly on optical absorption, luminescence and decay measurements. These interesting hosts are used due to their remarkable characteristics and applications on solid state lasers, solar concentrators, optical detectors, waveguide lasers, optical fibers for telecommunication and opto-electronics devices [1-4]. Tellurite glasses possess good chemical durability, good thermal and mechanical stability, high refractive index, good transparency in mid-infrared region (0.36-6 μm), low phonon energy (700-800 cm^{-1}), low melting temperature, high linear and nonlinear refractive index, excellent transmittance in visible and near-infrared region, wide transmission window (0.4-6 μm) and high solubility for RE ions [5-6]. It is well known that pure TeO_2 chemical does not form a glass on their own but when it is mixed with certain modifier Li_2CO_3, MgO, PbO and Nb_2O_5 etc, to become glass. The addition of Li_2CO_3 as network modifier, could enhance thermal, optical and electrical properties [5,7]. The addition of Nb_2O_5 as modifier could further improve the optical nonlinearity, vitrification and glass stability [7-10].

Non-destructive testing (NDT) of materials are commonly performed to identify, characterize, assess voids, defects and damage in materials [11]. The laws of physics that govern the propagation of high frequency sound waves through solid materials have been used to detect internal and surface discontinuities [12-13], thickness measurements [14-15] and analyzing material properties [16]. Ultrasonic testing techniques involve the propagation and detection of mechanical vibrations that have interacted in some way with the structure under test [17].

The NDT characterization of materials is a versatile tool for investigating the change in microstructure, deformation process, ultrasonic velocity, evaluation of elastic behaviour, morphological features and mechanical properties of materials over a wide range of temperatures [17]. The propagation of ultrasonic waves in solids such as glass provides valuable information regarding the solid state motion in the material [18]. It is also due to the availability of different frequency range and many mode of vibration of the ultrasonic waves to probe into the macro, micro and submicroatomic levels [19]. On the basis mode of ultrasonic wave propagation, there are four types of ultrasonic velocities which are longitudinal, shear, Rayleigh (surface) and Lamb (plate) wave velocity. However, the longitudinal and shear wave velocities are more important for the material characterization because they are well related to the elastic constant and density. The mechanical behaviour of the material can be well defined on the knowledge of ultrasonic velocity [20].

Sound waves are simply organized mechanical vibrations that travel through a medium at a specific speed or velocity, in a predictable direction. The longitudinal velocity of sound waves varies depending on the medium through which it is travelling, affected by the medium elastic properties and density. As they encounter a sudden change in different acoustic impedance, the sound waves will reflect and transmit. The extent of the reflection depends on the difference in acoustic impedance at the location where the higher the difference, the more the energy reflected [21]. As the sound beam propagated through the material, there will be a reduction in sound intensity known as attenuation. The attenuation of sound wave is due to the absorption, scattering, beam spreading, diffraction and other mechanisms that take place only after the acoustic energy enters the second medium [22]. The amount of energy lost through absorption depends upon the elastic properties of the material being tested [23] while loss due to scattering in materials also depends on the ratio of grain size and wavelength [16].

Glasses are a material with unique properties such as high hardness and transparency at room temperature, along with sufficient strength and excellent corrosion resistance. Due to possible applications in various technological and engineering fields, the study of glass characterization is of great significance. Glassy materials have acknowledged advantages such as physical isotropy and the absence of grain boundaries [24]. The applications of tellurite based glasses have been the subject of high interest nowadays due to their interesting electrical, optical and magnetic properties. Besides having a unique structure, tellurite glasses also have good mechanical strength, chemical durability and low melting temperature [25].

The elastic properties of glasses are of considerable significance, because the studies yield information concerning the forces that are operative between the atoms comprising as the solid. Hence, the elastic properties are suitable for describing the glass structure [26]. The elastic properties, Poisson's Ratio, microhardness, Debye temperature and softening temperature are important material properties to investigate the linear and anomalous variation as a function of the glass composition and have been interpreted in terms of structure or transformation of cross- linkages in the glass network [27].

This paper examines the effect of the concentration of Ag NPs embedded in Er^{3+}/ Nd^{3+} codoped lithium niobate tellurite glasses on the mechanical properties via non-destructive testing of prepared glass samples using melt quenching method. The Ag NPs concentration mediates improved the absorbance of the glass. The acoustic impedance and ultrasonic attenuation are calculated.

2. Materials and Methods

The Er^{3+}/Nd^{3+} doped glasses of the form (69-x)TeO_2-15Li_2CO_3-15Nb_2O_5-1Er_2O_3-(x)Nd_2O_3 with $0.2 \leq x \leq 1.0$ mol % are synthesized via conventional melt-quenching technique. Batch of 15 g raw materials from reagent grade powder of TeO_2 (purity 99%), Li_2CO_3 (purity 99%), Nb_2O_5 (purity 99%), Er_2O_3 (purity 99.9%) and Nd_2O_3 (purity 99.9%) are well mixed. The well-mixed powder is then melted in a platinum crucible at 900 °C for 30 minutes in an electric furnace. The sample is then quenched between two steel plates followed by annealing at 300 °C for 3 hours before slowly cooled down to the room temperature.

The ultrasonic experiment employs the pulse echo technique. The ultrasonic pulse is generated by pulser/receiver generator of United NDT ISONIC 2020 instrument. The pulse is then converted into an electrical signal and transmitted through the sample by straight beam contact transducer (KB-Aerotech, 2.25 MHz) and also the shear beam contact transducer (GB-MWS60°-4MHz) where the reflected from the back or inside surface of the sample. The reflected signal is detected and converted back into ultrasonic pulse by the transducer. After that, it is sent back to the pulser receiver generator and displayed on the ISONIC 2020 screen. Figure 1 shows the schematic diagram of typical ultrasonic pulse echo technique. The measurements of ultrasonic velocities; longitudinal and shear, were repeated thrice to check the accuracy of the data obtained.

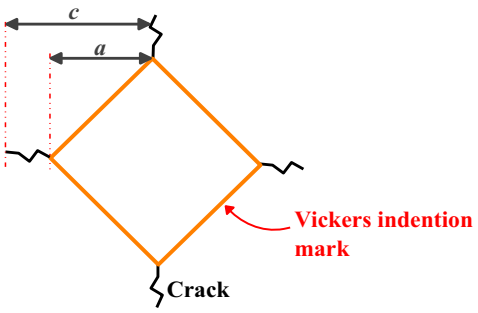

Figure 1. Vickers indention mark.

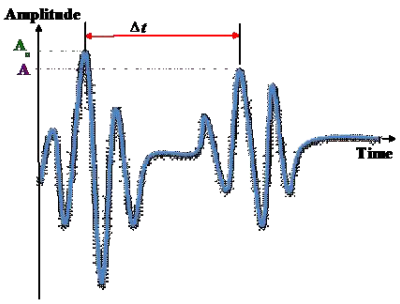

Figure 2. Typical time domain signal of ultrasonic wave propagation in a sample.

Figure 2 shows the typical time domain signal of ultrasonic wave propagation in a sample. The displayed signal represent the first and second backwall echoes are analyzed to determine the acoustic properties of the glass sample which are longitudinal velocity (v_l), shear velocity (v_s), mean velocity (v_{mean}), acoustic impedance (Z_{IM}) and attenuation coefficient (α). The longitudinal velocity, v_l and shear velocity , v_s are calculated from the sample thickness, d and difference transit time for first and second backwall echoes, Δt using [29]:

$$v_l = \frac{2d}{\Delta t_l} \tag{1}$$

$$v_s = \frac{2d}{\Delta t_s} \tag{2}$$

The acoustic impedance Z_{IM} is determined from the density, ρ and velocity, v of the glass sample by using [30]:

$$Z_{IM} = \rho v_{mean} \tag{3}$$

where $v_{mean} = \left[\frac{1}{3}\left(\frac{2}{v_s^{\,3}} + \frac{1}{v_l^{\,3}}\right)\right]^{\frac{1}{3}}$.

The attenuation coefficient, α of the sample is calculated from [31]:

$$\alpha = \frac{20\log_{10}\left(\frac{A_o}{A}\right)}{2d} \tag{4}$$

where A_o is the attenuated amplitude for first backwall echo and A is the attenuated amplitude for second backwall echo.

The elastic moduli of longitudinal (L), shear (G), bulk (B), Young's (E) are calculated from [32-35]:

$$L = \rho v_l^{\,2} \tag{5}$$

$$G = \rho v_s^{\,2} \tag{6}$$

$$B = L - \left(\frac{4}{3}\right)G \tag{7}$$

$$E = (1+\sigma)2G \tag{8}$$

where Poisson's ratio, $\sigma = \frac{(L-2G)}{2(L-G)}$.

The Debye temperature (θ_D) are calculated [32-34]:

$$\theta_D = \left(\frac{h}{k_b}\right)\left(\frac{3PN_A}{4\pi V_m}\right)^{\frac{1}{3}} v_{mean} \tag{9}$$

where h is Planck's constant, k_b is Boltzmann's constant, N_A is Avogadro number, V_m is molar volume calculated from molecular mass, M and density, ρ of the glass (i.e. M/ρ) and P is the number of atoms in chemical formula [32-34].

In addition, the theoretical micro-hardness (H_{th}) and softening temperature (T_s) are also calculated [32-35]:

$$H_{th} = (1-2\sigma)\frac{E}{6(1+\sigma)} \tag{10}$$

$$T_s = \left(\frac{M_a}{C\rho}\right)v_s^{\,2} \tag{11}$$

where M_a is the molecular weight of the glass (g/mol), the constant C of proportionality is equal to 507.4 $ms^{-1} K^{1/2}$ [30]. Thermal expansion coefficient (α_p) can be obtained as:

$$\alpha_p = 23.2\left(v_l - 0.57457\right) \tag{12}$$

Vickers hardness is measured by determining the diagonal lengths of an indent that occur when a diamond pyramid indenter with a specified load is applied into the sample material measured by using Shimadzu micro-hardness tester with test load 980.7 mN (0.1 H_v) for 15 second. From deformation-fracture patterns in Vickers indenter tests, the Vickers hardness, H_v for the glasses are evaluated by using equation [36]:

$$H_v = 1.854\frac{P}{D^2} \tag{13}$$

where P is the applied indention load (Newton) and D is the measured indention diagonal.

Fracture toughness, K_{IC} is one the macroscopic properties that characterize the fragility of a material. The fracture toughness of the samples is determined from the indention fracture using Vickers micro-hardness tester. A typical Vickers indention marks is shown in Figure 1. K_{IC} is calculated using the following equation [37],

$$K_{IC} = 0.016H_v\frac{a^2}{c^{3/2}} \tag{14}$$

where a is the half length of diagonal of the indent and c is the crack length from the center of the indentation to the crack end.

Brittleness, B of glass is the ratio of Vickers hardness to the fracture toughness and calculated using the following equation [38-39],

$$B = \frac{H_v}{K_{IC}} \tag{15}$$

The measuring the attractive or repulsive forces between the tip and sample are measured using Atomic Force Microscope ARIS, Model 3300. The experiment was carried out on a glass bulk sample, highly transparent and shiny glass samples of thickness ~2 mm.

3. Results and Discussion

3.1. Surface Plasmon Resonance

It is well known that the absorption in the UV-Vis spectra is the most reliable tool to analyze the function of metallic nanoparticles and observing the existence of surface plasmon resonance (SPR) band [40]. Figure 3 shows the absorption spectrum of glass without both dopant of Er^{3+} and Nd^{3+} ion. This shows the surface plasmon resonance (SPR) of the TLNA sample which confirms the existence of nanosize silver particles in glass matrix. The SPR bands centered at 558 nm and 597 nm is observed corresponding to the transverse and the longitudinal SPR oscillations of the Ag NPs, respectively. The strong absorption band shows the characteristics of fine metallic particles in a dielectric medium [41].

As the dielectric function of Ag NPs and the refractive index of glass system weigh, the SPR band of the isolated Ag NPs can be located. Based on the report previously, the SPR band observation of the isolated Ag NPs is in the region of 400-500 nm [42-44]. The significantly red shifted as compared to the classic one is observed related to different refractive index in the glass system where the position of the plasmon band is compared and positioned in the visible region [44]. This might be due to the higher refractive index possess by most tellurite glasses which normally lie approximately in the range of 2.0 to 2.5 [45-48].

This is particularly reliable since the higher refractive index will cause the SPR to shift to a longer wavelength [49-50]. It should however be noted out that the intensity of the SPR peaks are not so immense. This is due to the existence of spherical and non-spherical types of Ag NPs in the glass matrix as appears in insert figure in Figure 3, previously. Furthermore, the absorption coefficient of the samples is expected to be very much higher than those in the form of thin film as suggested by El-Hagary *et. al.* [51]. The existence of various sizes and shapes of Ag NPs are highly potential for generating a shift in SPR wavelength via overlap between plasmon [52-53].

The excitation of localized surface plasmon (LSP) by an electric field (light) at an incident wavelength where resonance occurs resulting in strong light scattering in the appearance of intense surface plasmon (SP) absorption bands and an enhancement of the local electromagnetic fields [54-56]. The maximum absorption and the intensity of SP absorption bands are the characterization of the silver material and it is a highly sensitive to size, size distribution and nanostructures to the environment surrounding them [54-55]. In addition, when considering the size effects, the SPR of Ag NPs smaller than about 5 nm lose much of their fine spectral features due to the broadening of plasmon bands. This effect is common in real silver nanoparticles synthesized by usual methods and it is stabilized by strong interacting ligands [42, 57].

Figure 4 revealed the topological variations of NPs in dielectrics to promote the local electric field further by lightening rod effects at the surface of spherical NPs which in turn enhanced the velocities (longitudinal and shear) of the ultrasonic analysis. The increase in both velocities shows the structure of the glass is more compact with the addition of Ag NPs in the glass system. Consequently, a correlation between an increase in the reflected echo intensity and the structural of the glass is established as shown in Figure 5.

3.2. Ultrasonic Analysis

Table 1 shows the ultrasonic properties of the (68-x)TeO_2-15Li_2CO_3-15Nb_2O_5-1Er_2O_3-1Nd_2O_3-(x)AgCl glass system. Ultrasonic non-destructive characterization of material is a versatile tool of inspection of their microstructures and their mechanical properties [58]. Moreover, it is possible due to the close association of the ultrasonic waves with the elastic and inelastic properties of the materials [58].

From Table 1, it can be seen that the density increases with the increasing concentration of Ag NPs from 5035 to 5047 kg/m^3. It is commonly known that the density of a material is very much depending on the molecular weight of that material [59]. In this case, the increase in density is due to the substitution of lower molecular weight AgCl (143.32 g/mol) by a higher molecular weight TeO_2 (159.60 g/mol). The higher in connectivity in the glass structure causes tighten in density as reported by others [60-61]. This increment is due to the increase in the compactness of the glass, presumable due to a formation of bridging oxygen [62]. Moreover, this is due to the fact that the number of Te-O linkages is increased which means the decrease in non-bridging oxygen in the glass network.

The ultrasonic velocity of longitudinal and shear are displayed in the Table 1 increased from 3542 to 3804 m/s and 2291 to 2532 m/s, respectively as the concentration of Ag NPs increases. Nadia *et.al.* states the larger concentration of metal oxide, the metal oxide ions cluster and a sort of de-mixing occurs [58]. Therefore, due to a small increase of Ag NPs in the glass system, the process of de-mixing between the Ag^+ ions and the strained Te-O linkages are happening. In addition, the Ag NPs embedded in the glass system are resulting in more close structures as in agreement with the increased in density. The close structures increase the resistance of the network deformation, resulting the structures are more rigid.

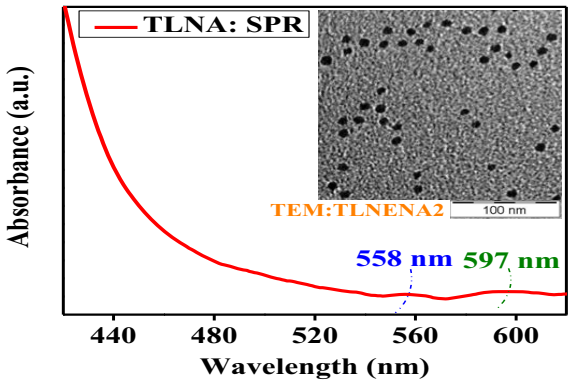

Figure 3. The surface plasmon band without dopant, Er^{3+} and Nd^{3+} ion of TLNA (insert: TEM image of TLNENA2).

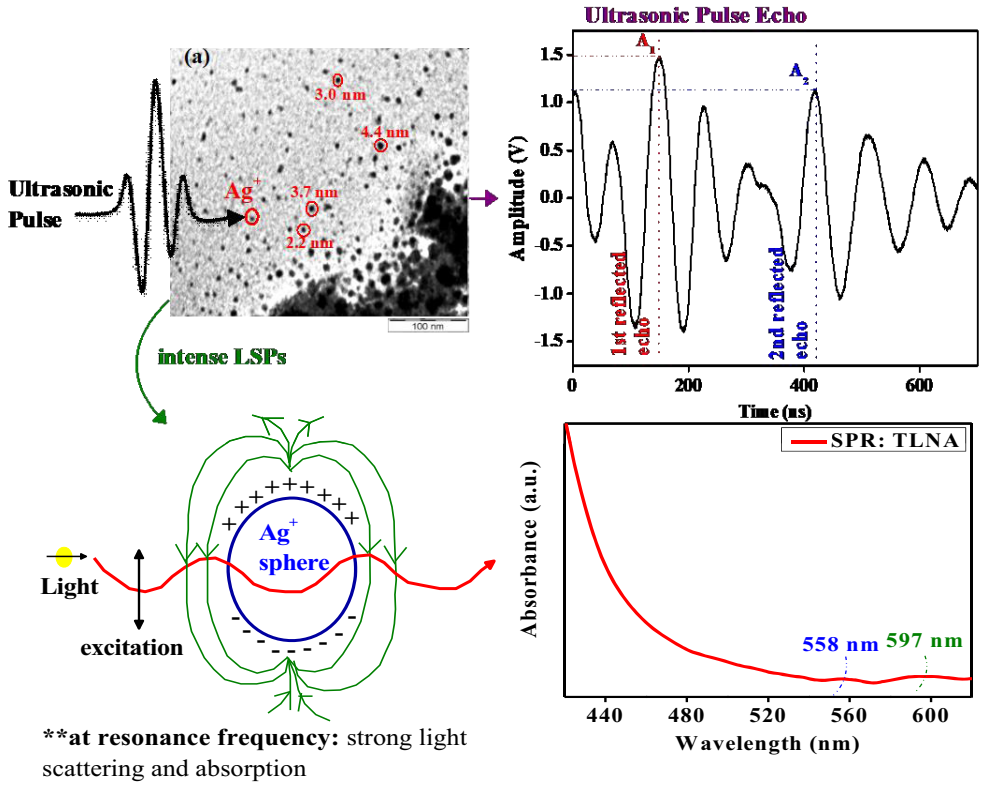

****at resonance frequency:** strong light scattering and absorption

Figure 4. Schematic diagram of Ultrasonic pulse in correlation with TEM analysis.

The acoustic impedance is increased from 15.36 to 16.91 ($\times 10^6$ kg/m^{2}s) as the Ag NPs concentration increased as it is complimentary with the density values. The attenuation coefficient of ultrasonic waves is due to absorption and scattering phenomena. The attenuation coefficient of the glass increased from 4.52 to 5.60 dB/cm as the Ag NPs concentration increased. The absorption converts the acoustic energy into heat. The absorption which converts acoustic field is irreversibly lost since it is dissipated in the medium where the absorption is essentially independent of particle size, shape and volume [16, 63]. In addition, scattering converts the energy of the coherent, collimated beam into incoherent, divergent waves which resulting with

the wave interaction with non-uniformities in the glass material. Moreover, the scattering from boundaries between small and randomly distributed particles (Ag NPs) in the glass system may create a small ripples in the reflected ultrasonic which is known as the structure noise where the noise limit detection of small cracks, pores (bubbles) or other discontinuities [63]. Therefore, as the attenuation coefficient increased, the absorption also increased as shown in Figure 6. As mentioned in previous paragraphs, the peak amplitude received is based on both velocity and attenuation coefficient of the glass where it is affected greatly by a minor difference in the microstructures of the glass system [64].

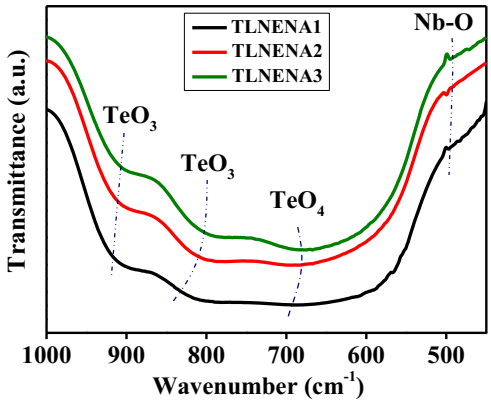

Figure 5. Infrared transmission spectra of TLNENA1, TLNENA2 and TLNENA3 glass sample.

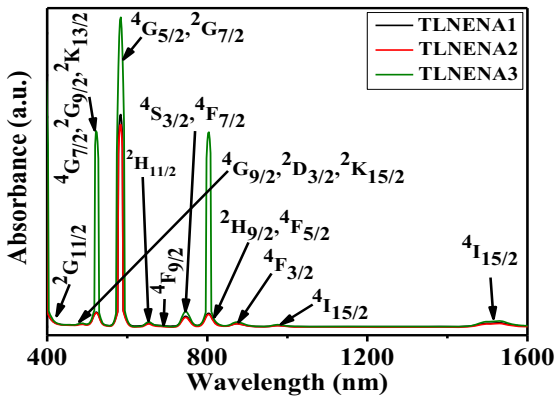

Figure 6. The UV-Vis-NIR absorption spectra the glass system.

Table 1. Density (ρ), Longitudinal velocity (v_l), Shear velocity (v_s), mean velocity (v_m), acoustic impedance (Z_{IM}) and attenuation coefficient (α) of TLNENA1, TLNENA2 and TLNENA3 glass sample.

Sample	ρ (±10 kg/m^3)	v_l (±11 m/s)	v_s (±12 m/s)	v_{mean} (±10 m/s)	Z_{IM} (±0.10 $\times 10^6$ kg/m^{2}s)	α (±0.04 dB/cm)
TLNENA1	5035	3542	2291	3051	15.36	4.52
TLNENA2	5039	3750	2481	3287	16.57	5.40
TLNENA3	5047	3804	2532	3350	16.91	5.60

Table 2 shown the computed values of longitudinal modulus (L), shear modulus (G), bulk modulus (B), Young's modulus (E), Poisson's ratio (σ), softening temperature (T_s) and thermal expansion coefficient (α_p). The L and G modulus increased from 63.17 to 73.03 GPa and 26.43 to 32.36 GPa, respectively, as the Ag NPs concentration increased. The increased of L and G are due to the formation of sufficient number of bridging oxygen, BO which caused the increased in rigidity and stiffness of the glass and offsets the effect of the increase in density on the velocities [34]. The L and G modulus showed a

similar behavior as the v_l and v_s, respectively where it is dominated by the changes in the independent modulus [34]. The B and E shown a slightly change where increases from 27.93 to 29.89 GPa and 60.27 to 71.33 GPa, respectively as the Ag NPs concentration increased.

The increased of elastic moduli: L, G, B and E is due to the formation of sufficient number of bridging oxygen (BO) could justify the increase in rigidity and stiffness of the glass sample and offsets the effect of increase in density [34]. The influence of BO on the elastic moduli with the addition of Ag NPs is evidenced in the FTIR results where the FTIR spectra (Figure 4) shown increase in the transmittance intensity. The TeO_4 and TeO_3 both shown increased in the transmittance intensity which indicates an increase of BO where influence the elastic moduli. Moreover, as the Ag NPs concentration increase, the larger the number of BO ions compared to the non-bridging oxygen (NBO) in the glass network. The intensity of Nb-O increased as the Ag NPs concentration increased as shown in Figure 5. It is suggests to more creation of Te-O-Nb linkages with the increasing of Ag NPs which contribute to the increased of connectivity of the glass network. Based on it, it indicates the increased in elasticity of the glass through the formation of stronger covalent Nb-O bonds [34].

Table 2. Experimental elastic moduli [longitudinal (L), shear (G), bulk (B) and Young's (E)], Debye temperature (θ_D), Poisson's ratio (σ), Softening temperature (T_s) and Thermal expansion coefficient (α_p) of TLNENA1, TLNENA2 and TLNENA3 glass sample.

Sample	L (GPa)	G (GPa)	B (GPa)	E (GPa)	θ_D (K)	σ	T_s (K)	α_p (×10^3 K^{-1})
TLNENA1	63.17	26.43	27.93	60.27	1773	0.14	342	82.16
TLNENA2	70.86	31.02	29.51	68.91	1909	0.11	400	86.99
TLNENA3	73.03	32.36	29.89	71.33	1946	0.10	416	88.24

To determine the atomic vibrations as the temperature at which all lattice vibration modes are excited is by calculate the Debye temperature, θ_D [34]. In addition, θ_D is an important parameter to confirm the elasticity and rigidity of the solid [35]. As shown in the eq. (9), the Debye temperature depends on the change of V_m, P and v_{mean} as the Ag NPs content increase in the glass system. Based on the calculation, as the V_m and P values decreases, the Debye temperature is increase as the Ag NPs increase together with v_{mean}. The behavior of v_{mean} and θ_D are closely similar, therefore as a conclusion the change in θ_D is dominated with the values of v_{mean} [33-34]. The increase of θ_D is due to the strength of the glass network structure as it increase of rigidity of the glass with the addition of Ag NPs in the glass system [33, 35]. It is complementary with the increase of density. The increase of rigidity of the glass can also be proving as the L and G also increases [35, 65].

Poisson's ratio is defined as the ratio between lateral and longitudinal strain produced when tensile force is applied and it is usually inversely proportional to density of cross links in the glass network [33]. Moreover, the Poisson's ratio is known as the expansion of the sample in perpendicular direction to an applied stress [65]. Based on the data calculated, Poisson's ratio is decrease as the Ag NPs content increased.

As previously stated, many oxide glasses including network former, TeO2 and network modifier such as Nb2O5 and Na2O have an approximate value σ = 0.2 where it is due to the formation of non-bridging oxygen runs parallel to reduction in dimensionality [35]. The highest Poisson's ratio is 0.14 where has the lowest Ag NPs (1 mol %) and it is in the agreement with other researchers [29-30, 35, 65]. When the mol concentration of Ag NPs increase in the glass system, the Poisson's ratio decreases where the concentration have the least destines of the glass series, allowing a large relaxation of the structure at the applying of the sound waves which makes the lateral (shear) strain becomes larger than the longitudinal strain [30].

Softening temperature, T_s is defined as the temperature point at which viscous flow changes to plastic flow where in actual practices, it plays a crucial role in determining the temperature stability of the glass. As the softening temperature of a glass increase from 342 K to 416 K, the stability of its elastic properties also increases [66]. Values of softening temperature for lithium niobate tellurite glasses were calculated and presented in Table 2. The softening temperature increases with the increasing of Ag NPs content. This shows that the stability of the glasses increases as the doping salt (metallic nanoparticles) content increases. This change is what may be expected from the increase of elastic moduli, L, G, B and E [66]. The thermal expansion coefficients, α_p increase from 82.16 to 88.24 $\times 10^3$ K^{-1} as Ag NPs content increases and listed in Table 2.

3.3. Atomic Force Microscopy Analysis

The surface structure of a glass is generally believed to control a variety of chemical and physical changes that occur during the preparation of the glass sample. Therefore, a better understanding is needed on the surface characteristics of glass samples. One technique that can provide high-resolution, three-dimensional imaging of material surfaces is atomic force microscopy (AFM). AFM requires no specific sample preparation procedure and provides information about the sample surface in a relatively non-destructive fashion. Another advantage of this technique is that imaging can be done in dry or in liquid environments [67].

The surface topography of (68-x)TeO_2+15Li_2CO_3+15Nb_2O_5+1Er_2O_3+1Nd_2O_3 +(x)AgCl glass system were taken by atomic force microscopy and the change of surface roughness (average and root-mean-square) with annealing temperature is presented in Figure 7 where (a, c, e) were 2D images and (b, d, f) were a 3D images. The AFM images indicate that both the surface roughness and the average size of the features increase with increasing of Ag NPs concentration. The size of the features is consistence with the average diameter size of Ag NPs gathered from the TEM images as shown in Table 3 agreed by other researchers previously [67-69].

Table 3. TEM size distribution and mean diameter of AFM of TLNENA1, TLNENA2 and TLNENA3 glass sample.

Sample	Average Ag NPs sizes in TEM (±0.01 nm)	Mean Ag NPs diameter in AFM (±0.01 nm)
TLNENA1	3.70	3.83
TLNENA2	3.50	3.34
TLNENA3	1.18	1.24

Figure 8 (a), (c) and (e) shows the TEM image of TLNENA1, TLNENA2 and TLNENA3 glasses, respectively where the black spots signify the occurrence of Ag NPs having different sizes and shapes. This indicates the nucleation of spherical and non-spherical NPs within the glass matrix. The existence of various

sizes and shapes of Ag NPs are highly potential for generating a shift in SPR wavelength via overlap between Plasmon resonance [52-53, 70-71]. During the melting processes first Ag^{+} ions are formed (from the dissociation of AgCl) and then reduced to Ag^{0} via redox reaction. Moreover, when considering the intrinsic size affects, the SPR of Ag NPs smaller than 5 nm is losing their fine spectral features due to the broadening of plasmon bands where this effect is common in Ag NPs [72-73]. Figure 8 (b), (d) and (f) The glass samples show irregular grains and bubbles on the surface due to cubic crystalline structure of the doping salt of Ag NPs. The Ag NPs are observed loosely bound cylindrical and tiny pyramid shape for the glass samples as the Ag NPs concentration increased from 1.0 to 3.0 mol% which may be the cause of the effect [67].

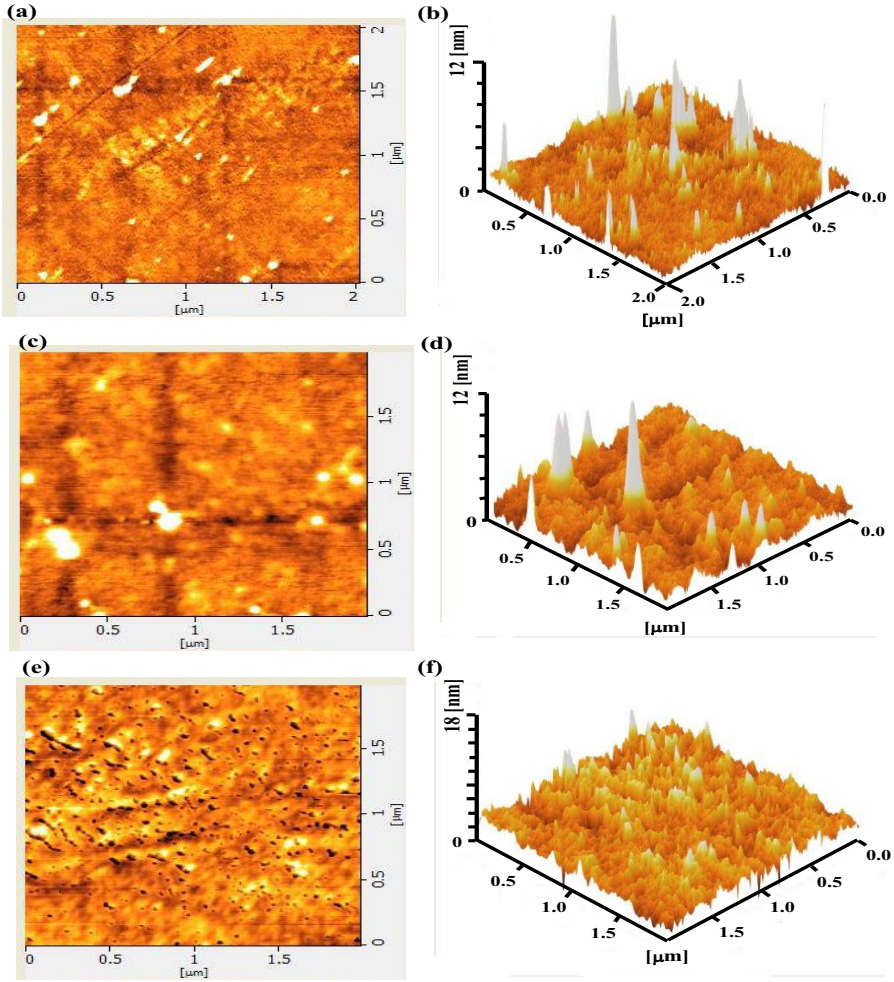

Figure 7. (a, c, e) the 2D images and (b, d, f) the 3D images of the glass samples.

Roughness parameters are being presented as obtained results of AFM analysis in Table 4 where R_a (arithmetic average roughness), R_p (maximum height of the profile/ maximum peak), R_z (mean height of roughness in ten points) and RMS (root mean square roughness) for the glass sample as the Ag NPs concentration increased. From presented results in the Table 4, it can be said that lowest values of roughness parameters have the lowest Ag NPs concentration as expected based on the TEM and contact angle analysis

whereas the Ag NPs concentration increases, the surface roughness also increases shown in the previous paper [74].

The average surface roughness of the glass sample is found in the range 0.86 to 4.40 nm and observed to increase with Ag NPs which indicates three-dimensional growth of the glass sample. The microstructure of these glass samples did not change significantly and the glass sample showed small grains with equiaxed (same dimensions) grain morphology and grain size is to be order of 0.86 to 4.40 nm. From the 3D images, it is observed that the size of the island is increased with the increase of Ag NPs concentration which may be attributed to the saturation of diffusion and recrystallization [69]. The TLNENA1 glass is observed to have larger and non-uniform grains as well as random orientation as compared to the TLNENA2 and TLNENA3 glass. The results are in accordance with the TEM average diameter size. The number of grains is also observed to increase with Ag NPs which indicated that the smaller grains tend to decrease in concentration as recrystallization become more effective [69]. A similar behavior of surface topography was reported by other researchers [68, 75-77].

As the size distribution of Ag NPs getting smaller as the Ag NPs concentration increases shows the surface roughness of the glass sample also increases and the water contact of the glass sample surface also increases as shown in previous paper [74]. It is due to the Ag NPs are distributed at all over the glass sample which brings to the confirmation of self-cleanliness ability of the Er^{3+}/ Nd^{3+} codoped lithium niobate tellurite glass embedded with Ag NPs.

3.4. Mechanical Properties

Table 5 shows the variation of measured theoretical micro-hardness (H_{th}), Vickers hardness (H_v), fracture toughness (K_{IC}) and the brittleness (B) of the glass samples as shown in Figure 9 and Figure 10. The values of H_{th} is increase from 2.94 to 3.60 GPa as the Ag NPs content increase. The steady increase of micro-hardness indicates the increased in stress needed to eliminate free volume as Ag NPs increased in the glass system [34]. Vickers hardness is increases as the Ag NPs content increase from 3.66 to 3.78 GPa. This can be attributed to the increase in resistance against the deformation with the increase distribution of the Ag NPs [47,78]. Both of the data H_{th} and H_v are in good agreement with θ_D which it may be attribute to the strength of the network structure as the rigidity of the glass increase [35].

Table 4. Surface roughness parameter of TLNENA1, TLNENA2 and TLNENA3 glass sample.

Sample	**Roughness parameter (±0.01 nm)**			
	R_a	R_p	R_z	*RMS*
TLNENA1	2.93	1.10	5.39	5.55
TLNENA2	4.37	2.84	6.27	7.19
TLNENA3	6.65	5.63	8.48	8.93

Table 5. Theoretical micro-hardness (H_{th}),Vickers hardness (H_v), fracture toughness (K_{IC}) and brittleness (B)of TLNENA1, TLNENA2 and TLNENA3 glass sample.

Sample	H_{th} **(±0.03 GPa)**	H_v **(± 0.01 GPa)**	K_{IC} **(MPa m$^{1/2}$)**	B **(μm$^{-1/2}$)**
TLNENA1	2.94	3.66	2.708	135.16
TLNENA2	3.45	3.68	3.544	103.96
TLNENA3	3.60	3.78	4.174	90.65

The crack initiation and crack propagation are the two main factors which are used to evaluate the strength of glass samples. Fracture toughness is defines the ease with which a crack can propagate through a material is used for the evaluation of crack propagation through the glasses. In addition, the crack initiation in glass samples is determined by calculating the brittleness index due to the crack initiation in material mainly depends on their brittleness [78].

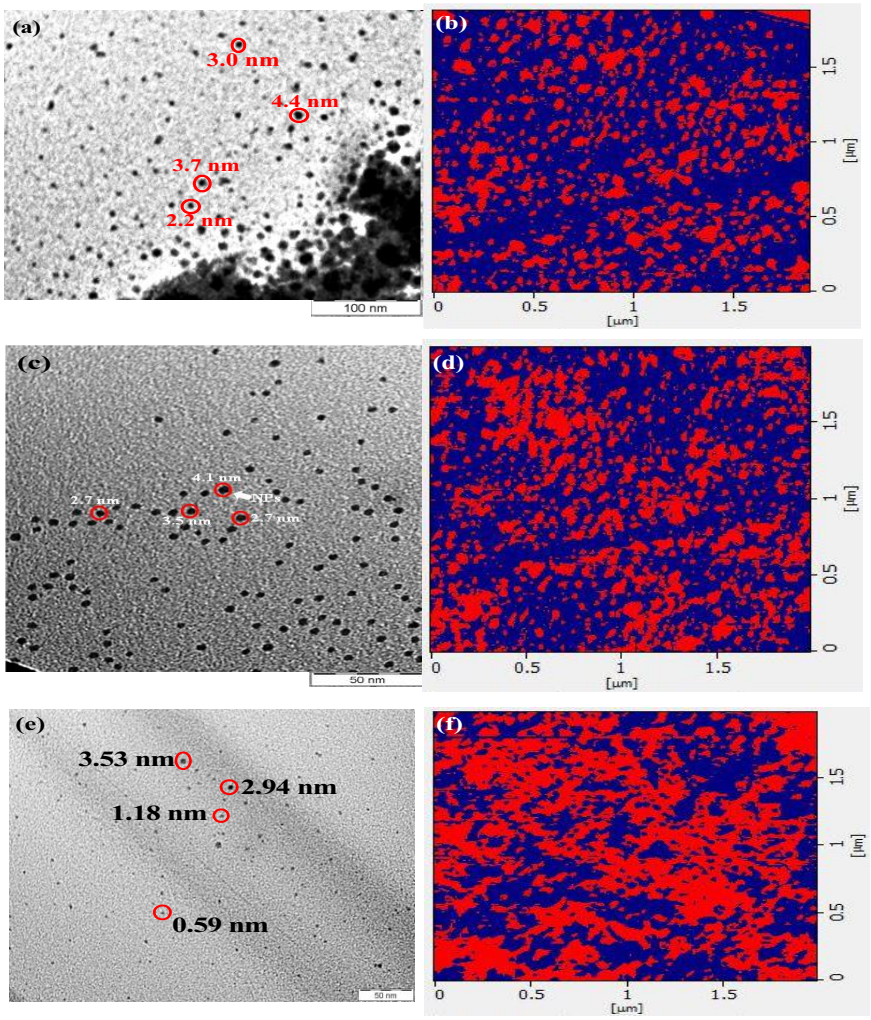

Figure 8. (a, c, e) the TEM images and (b, d, f) the AFM images of grain Ag NPs of TLNENA1, TLNENA2 and TLNENA3 glass sample

Fracture toughness values of the glass samples increases as Ag NPs content increase from 2.708 to 4.174 MPa $m^{1/2}$. The increase in Vickers hardness and decrease in measured crack length, results the marginal increase in the fracture toughness of glass samples with the increase of Ag NPs content. Moreover, reduction in the crack length is explained using the concept of generation of compressive stress around the particles present in the glass matrix due to the rapid quenching of the glass melting [78]. Thermal expansion mismatch between glass matrix and metal particles during rapid quenching of glass melt from the high processing

temperature leads to the generation of compressive stress around the particles in the glass matrix. These stresses are compressive in the glass matrix and tensile in the particles. The compressive stress in the glass matrix increases whereas tensile stress of metal particles decreases with increased in distribution of these metal particles, Ag NPs. When generated, the radial-median crack due to Vickers indentations encounter Ag NPs, the crack front penetrates first between the particles and once it reaches a critical penetration depth, it overcomes the trapping effect and start propagating again. This reduces the crack propagation through the Ag NPs embedded glasses [78-79]. Hence thermal residual stresses improve the mechanical properties of Ag NPs embedded lithium niobate tellurite glass codoped Er^{3+}/ Nd^{3+}.

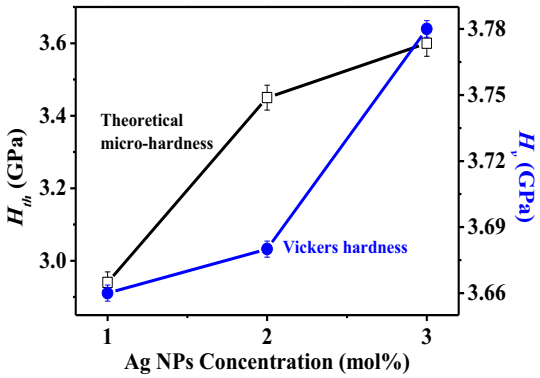

Figure 9. Theoretical micro-hardness and Vickers hardness against Ag NPs concentration.

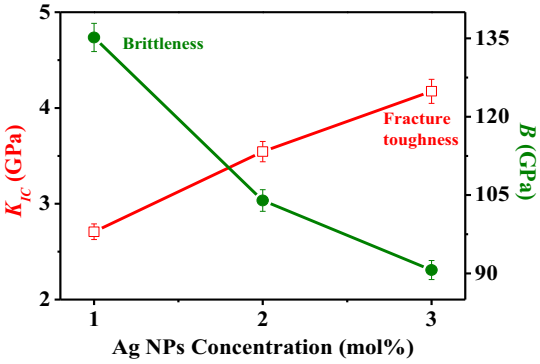

Figure 10. Fracture toughness and brittleness against Ag NPs concentration.

Small reductions in brittleness observed for the glass samples as it is decreases from 135.16 to 90.65 $\mu m^{-1/2}$ as the Ag NPs content increases is attributed to the improvement in plastic flow caused by the formation and growth of silver nanoparticles in the lithium niobate tellurite glass codoped Er^{3+}/ Nd^{3+} glass matrix [78-80]. Brittleness of glasses depends on densification and plastic flow modes of deformation before the crack initiation process.

In conclusion, the results clearly showed the increase in distribution of Ag NPs, the shorter the median crack length of the glass samples. Therefore, the presence of thermal residual stress is considered as the toughening and strengthening mechanisms in the improvement of mechanical properties observed experimentally.

4. Conclusions

The ultrasonic, surface, mechanical, optical and photocatalysis properties of Ag NPs incorporated LNT glass with Er^{3+}/ Nd^{3+} co-doping are determined. As the Ag NPs content increase, the ultrasonic properties: longitudinal modulus (L), shear modulus (G), bulk modulus (B), Young's modulus (E) and Debye temperature (θ_D) were observed to be increase. FTIR showed formation of both bridging oxygen (BO) and non-bridging oxygen (NBO), but the former was found to be more dominant. It is suggested that recovery of rigidity of the glass system was due to formation of bridging oxygen as a result of Ag NPs addition. The surface roughness of the glass sample is in the range of 0.39 to 4.40 nm and observed to increase with Ag NPs which indicates three-dimensional growth of the glass sample as the AFM analysis shown. The mechanical properties of the glass sample displayed the strong influence of Ag NPs on the glass structure.

The relationship between Ag NPs concentration on ultrasonic, surface and mechanical properties is established. These findings may be useful in the development of promising environment glass application.

Acknowledgments
We gratefully acknowledge the financial support from Ministry of Higher Education through grant UTMER Vot. 17J86 of Universiti Teknologi Malaysia and the experimental assistance from Faculty of Science.

References

[1] Serqueira E.O., Dantas N.O., Monte A.F.G., Bell M.J.V., Judd Ofelt Calculation of Quantum Efficiencies and Branching Ratios of Nd^{3+} Doped Glass, Journal of NonCrystalline Solids 352 (2006) 3628-3632.

[2] Selvaraju K., Marimuthu K., Structural and Spectroscopic Studies on Concentration Dependent Sm^{3+} Doped Boro-Tellurite Glasses, Journal of Alloys and Compound 553` (2013)273-281.

[3] Ravi O., Reddy C.M., Manoj L., Raju B.D.P., Structural and Optical Studies of Sm^{3+} ions Doped Niobium Borotellurite Glasses, Journal of Molecular Structure 1029 (2012) 53-59.

[4] Mahraz Z.A.S., Sahar M.R., Ghoshal S.K., Enhanced Luminescence from Silver Nanoparticles Integrated Er^{3+} - Doped Boro-Tellurite Glasses: Impact of Annealing Temperature, Journal of Alloys and Compounds 649 (2015) 1102-1109.

[5] Raju K.V., Raju C.N., Reddy B.S., Judd-Ofelt Analysis and Photoluminescence Properties of RE^{3+} (RE=Er & Nd): Cadmium Lithium Boro Tellurite Glasses, Solid State Sciences 15 (2013) 102-109.

[6] Mahraz Z.A.S., Sahar M.R., Ghoshal S.K., Dousti M.R., Concentration Dependent Luminescence Quenching of Er^{3+} -Doped Zinc Boro-Tellurite Glass, Journal of Luminescence 144 (2013) 139-145.

[7] Nurhafizah H., Rohani M.S., Ghoshal S.K., Er^{3+}: Nd^{3+} concentration dependent spectral features of lithium-niobate-tellurite amorphous media, Journal of Non-Crystalline Solids 443 (2016) 23-32.

[8] Udovica M., Thomasa P., Mirgorodskya A., Massona O., Merle-Mejeana T., Lasbrugnasa C., Champarnaud-Mesjarda J.C., Hayakawa T., Formation Domain and Characterization of New Glasses Within the Tl_2O-TiO_2-TeO_2 System, Materials Research Bulletin 44(2) (2009) 248-253.

[9] Lin J., Huang W., Sun Z., Ray C.S., Day D.E., Structure and Non-Linear Optical Performance of TeO_2-Nb_2O_5-ZnO Glasses, Journal of Non-Crystalline Solids 336 (3) (2004) 189-194.

[10] Rivero C., Stegeman R., Couzi M., Talaga D., Cardinal T., Richardson K., Stegeman G., Resolved Discrepancies between Visible Spontaneous Raman Cross Section and Direct Near Infrared Raman Gain Measurements in TeO_2-Based Glasses, Optics Express 13(12) (2005). 4759 -4769.

[11] Berke M., Hoppenkamps U., Nondestructive Material Testing with Ultrasonics (3rd Ed.). Krautkrämer Training System Level 1 (1990).

[12] Chung S.M., The Interactions of Ultrasonic Rayleigh Waves with Surface Discontinuities in Steel, Iowa State University: PhD Thesis (1984).

[13] Bernard M., Ultrasonic Surface Crack Characterization Using Rayleigh Waves, Swiss Federal Institue of Technology Zurich: PhD Thesis (2006).

[14] Kenneth A.F., Gerry M.E., Karen A.S., Thomas J.N., Theory and Application of Precision Ultrasonic Thickness Gaging, Journal of British Institute of Non- Destructive Testing 2(10) (1997).

[15] Thompson D.O., Chimenti D.E., Ultrasonic Measurement of Pipe Thickness, New York: Plenum

Press (1993).
[16] Nanekar P.P., Shah B.K., Characterization of Material Properties by Ultrasonics. BARC Newsletter 249 (2003)25-38.
[17] Robert L., The Improvement of Ultrasonic Apparatus for The Routine Inspection of Concrete, Imperial College of Science, Technology and Medicine: PhD Thesis (2000).
[18] Hesham A., Samier M., Ultrasonic Velocity and Elastic Moduli of Heavy Metal Tellurite Glasses, Journal of Materials Chemistry and Physics 80 (2003) 517-523.
[19] Kannappan A.N., Thirumaran S., Palani R., Elastic and Mechanical Properties of Glass Specimen by Ultrasonic Method, ARPN Journal of Engineering and Applied Sciences 4 (1) (2009) 27-31.
[20] Rajendran V., Palanivelu N., Chaudhuri B.K., Goswami K., Characterisation of Semiconducting V_2O_5-Bi_2O_3-TeO_2 Glasses through Ultrasonic Measurements, Journal of Non-crystalline Solids 320 (2003) 195-209.
[21] Don W.D., Acoustic Waves, Croatia: Sciyo Press (2010).
[22] Alvar C.E., Market Analysis for A Long Range Ultrasonic Inspection Program of The Enterprise Areva, Ansbach University of Applied Science: Master Thesis (2012).
[23] Bindal V.N., Water-Based Couplants for General Purpose Use for Ultrasonic NDT Applications, Journal of Scientific & Industrial Research 59 (2000) 935-939.
[24] Drury J.C., Ultrasonic Flaw Detection for Technician (4th Ed.), Rawlings Rd, Llandybïe: Salesbury Press (1984).
[25] M.K. Halimah, W.M. Daud, H.A.A. Sidek, A.W. Zaidan, A.S. Zainal, Optical Properties ofTernary Tellurite Glasses, Journal of Materials Science -Poland 28 (1) (2010) 173-180.
[26] Mohamed N.B., Yahya A.K., Deni M.S.M., Mohamed S.N., Halimah M.K., Sidek H.A.A., Effects of concurrent TeO_2 reduction and ZnO addition on elastic and structural properties of (90-x)TeO_2-10Nb_2O_5–(x)ZnO glass, Journal of Non-Crystalline Solids 356 (2010) 1626-1630.
[27] Thirumaran S., Jayakumar J.E, Ultrasonic and Spectroscopic Studies on Structural Elucidation of Some Vanadium Glasses, Research Journal of Physics 8(1) (2014) 1-16.
[28] L. Raewat, B.Cherdsak, Characterization of Elastic and Structural Properties of Alkali Borosilicate Glasses Doped with Vanadium Oxide Using Ultrasonic Technique, Glass Physics and Chemistry 41(4) (2015) 352-358.
[29] El-Mallawany R., Afifi H., Elastic moduli and crosslinking of some tellurite glass systems, Materials Chemistry and Physics 143 (2013) 11-14.
[30] Elkhoshkhany N., El-Mallawany R., E. Syala, Mechanical and thermal properties of TeO_2-Bi_2O_3-V_2O_5-Na_2O-TiO_2 Glass System, Ceramics International 42 (2016) 19218-19224.
[31] Rajendran V., Palanivelu N., Chaudhuri B.K., Goswami K., Characterisation of semiconducting V_2O_5-Bi_2O_3-TeO_2 glasses through ultrasonic measurements, Journal of Non-Crystalline Solids 320 (2003) 195-209.
[32] Afifi H., Samier M., Ultrasonic velocity and elastic moduli of heavy metal tellurite glasses, Materials Chemistry and Physics 80 (2003) 517-523.
[33] Umair M.M., Yahya A.K., Elastic and structural changes of $x$$Na_2O$-(35-$x$)$V_2O_5-65TeO_2$ glass system with increasing sodium, Materials Chemistry and Physics 142 (2013) 549-555.
[34] Azianty S., Yahya A.K., Enhancement of elastic properties by WO_3 partial replacement of TeO_2 in ternary (80-x)TeO_2-20PbO-$x$$WO_3$ glass system, Journal of Non-Crystalline Solids 378 (2013) 234-240.
[35] Yousef E.S., Elokr M.M., AbouDeif Y.M., Optical, elastic properties and DTA of TNZP host tellurite glasses doped with Er^{3+} ions, Journal of Molecular Structure 1108 (2016) 257-262.
[36] Shannon, R.D.T.,Prewitt, C.T., Effective ionic radii in oxides and fluorides, Acta

Crystallographica Section B: Structural Crystallography and Crystal Chemistry 25 (1969) 925-946.
[37] Zawrah, M.F., Essawy, R.A., Zayed, H.A., Fattah, A.H.A., Taha, M.A., Mechanicalalloying, sintering and characterization of Al_2O_3–20wt%–Cu nanocomposite, Ceramics International 40 (2014) 31-38.
[38] Rao G.V., Shashikala H.D., Optical, dielectric and mechanical properties of silver nanoparticle embedded calcium phosphate glass, Journal of Non-Crystalline 402 (2014) 204-209.
[39] Manoj K.N., Shashikala H.D., Optical absorption, mechanical properties and FTIR studies of silver-doped barium phosphate glasses, Physics and Chemistry of Glasses: European Journal of Glass Science & Technology Part B 57(2) (2016) 90-96.
[40] Amjad R. J., Sahar M. R., Ghoshal S. K., Dousti M. R., Riaz S., Tahir B. A., Enhanced Infrared to Visible Upconversion Emission in Er^{3+} doped Phosphate Glass: Role of Silver Nanoparticles, Journal of Luminescence 132 (2012) 2714-2718.
[41] Willets K.A., Duyne R.P.V., Localized Surface Plasmon Resonance Spectroscopy and Sensing, The Annual Review of Physical Chemistry 58 (2007) 267-297.
[42] Lee K.C., Lin S.J., Lin C.H., Tsai C.S., Lu Y.J., Size Effect of Ag Nanoparticles on Surface Plasmon Resonance, Surface & Coatings Technology 202 (2008) 5339 -5342.
[43] Smitha S.L., Nissamudeen K.M., Philip D., Gopchandran K.G., Studies on Surface Plasmon Resonance and Photoluminescence of Silver Nanoparticles, Spectrochimica Acta Part A 71 (2008) 186-190.
[44] Zakaria R., Hamdan K.S., Noh S.M.C., Supangat A., Sookhakian M., Surface Plasmon Resonance and Photoluminescence Studies of Au and Ag Micro Flowers, Optical Society of America (2015) 1-8.
[45] Yousef E., Hotzel M., Russel C., Linear and Non-Linear Refractive Indices of Tellurite Glasses in the System TeO_2–WO_3–ZnF_2, Journal of Non-Crystalline Solids 342 (2004) 82-88.
[46] Sakida S., Nanba T., Miura Y., Refractive-index Profiles and Propagation Losses of Er^{3+} doped Tungsten Tellurite Glass Waveguide by Ag^+–Na^+ ion exchange, Materials Letters 60 (2006) 3413-3415.
[47] Pavani P. G., Suresh S., Mouli V. C., Studies on Boro Cadmium Tellurite Glasses, Optical Materials 34 (2011) 215-220.
[48] Pavani P. G., Sadhana K., Mouli V. C., Optical, Physical and Structural Studies of Boro Zinc Tellurite Glasses, Physica B 406 (2011) 1242-1247.
[49] Mulvaney P., Surface Plasmon Spectroscopy of Nanosized Metal Particles, Langmuir 12 (1996) 788-800.
[50] Som T., Karmakar B., Nanosilver Enhanced Upconversion Fluorescence of Erbium ions in Er^{3+}: Ag-Antimony Glass Nanocomposites, Journal of Applied Physics 105 (2009) 013102 (8p.).
[51] El-Hagary M., Emam-Ismail M., Shaaban E. R., Shaltout I., Optical Properties of Glasses (TeO_2–GeO_2–K_2O) Thin Films co-doped with Rare Earth Oxides Sm_2O_3/Yb_2O_3, Journal of Alloys and Compounds 485 (2009) 519-523.
[52] Dousti R.M., Sahar M.R., Ghoshal S.K., Amjad R.J., Samavati A.R., Effect of AgCl on Spectroscopic Properties of Erbium doped Zinc Tellurite Glass, Journal of Molecular Structure 1035 (2013) 6 – 12.
[53] Rozra J., Saini I., Aggarwal S., Sharma A., Spectroscopic Analysis of Ag Nanoparticles Embedded in Glass, Advanced Materials Letter 4 (2013) 598-604.
[54] Mock J.J., Barbic M., Smith D.R., Schultz D.A., Schultz S., Shape Effects in Plasmon Resonance of Individual Colloidal Silver Nanoparticles, Journal of Chemical Physics 116 (2002) 6755-6759.
[55] Hutter E., Fendler J.H., Exploitation of Localized Surface Plasmon Resonance, Advanced Materials

16(19) (2004) 1685-1706.
[56] Willets K.A., Duyne R.P.V., Localized Surface Plasmon Resonance Spectroscopy and Sensing, The Annual Review of Physical Chemistry 58 (2007) 267-297.
[57] Amendola V., Bakr O.M., Stellacci F., A Study of the Surface Plasmon Resonance of Silver Nanoparticles by the Discrete Dipole Approximation Method: Effect of Shape, Size, Structure and Assembly, Plasmonics 5 (2010) 85-97.
[58] Nadia S.A.E., Hesham A.A., Structure and Ultrasonic Properties of Vanadium Tellurite Glasses Containing Copper Oxide, Archives of Acoustics 34(4) (2009) 641-654.
[59] Damas P., Coelho J., Hungerford G., Hussain N.S., Structural Studies of Lithium Boro Tellurite Glasses doped with Praseodymium and Samarium Oxides, Materials Research Bulletin 47 (2012) 3489-3494.
[60] Chowdari B. V. R., Kumari P. P., Studies on Ag_2O, M_xO_y. TeO_2 (M_xO_y = WO_3, MoO_3, P_2O_5 and B_2O_3) Ionic Conducting Glasses, Solid State Ionics 113-115 (1998) 665-675.
[61] Pavani P. G., Sadhana K., Mouli V. C., Optical, Physical and Structural Studies of Boro Zinc Tellurite Glasses, Physica B 406 (2011) 1242-1247.
[62] Sokolov V.O., Plotnichenko V. G., Koltashev V.V., Structure of Barium Chloride-oxide Tellurite Glasses, Journal of Non-Crystalline Solids 355 (2009) 1574-1584.
[63] Kazys R., Tumsys O., Pagodinas D., A New Ultrasonic Technique for Detection and Location of Defects in Three-Layer Plastic Pipes with a Reinforced Internal Layer, Ultragarsas (Ultrasound) 63(3) (2008) 19-27.
[64] Shen Q., Omar M., Dongri S., Ultrasonic NDE Techniques for Impact Damage Inspection on CFRP Laminates, Journal of Materials Science Research 1(1) (2012) 2-16.
[65] Mohamed N.B., Yahya A.K., Deni M.S.M., Mohamed S.N., Halimah M.K., Sidek H.A.A., Effects of Concurrent TeO_2 Reduction and ZnO Addition on Elastic and Structural Properties of (90-x)TeO_2-10Nb_2O_5-(x)ZnO glass, Journal of Non-Crystalline Solids 356 (2010) 1626-1630.
[66] Sidek H.A.A., Rosmawati S., Azmi B.Z., Shaari A.H., Effect of ZnO on the Thermal Properties of Tellurite Glass, Advances in Condensed Matter Physics (2013) 1-6.
[67] Gu X., Raghavan D., Nguyen T., VanLandingham M.R., Yebassa D., Characterization of Polyester Degradation Using Tapping Mode Atomic Force Microscopy: Exposure to Alkaline Solution at Room Temperature, Polymer Degradation and Stability 74 (2001) 139-149.
[68] Rahman K.S., Haque F., Islam M.A., Alam M.M., Effect of Growth Techniques on the Properties of CdTe Thin Films for Photovoltaic Application, IEEE Student Conference on Research and Development (2013) 265-268.
[69] Chander S., Dhaka M.S., Optimization of Physical Properties of Vacuum Evaporated CdTe Thin Films with the Application of Thermal Treatment for Solar Cells, Materials Science in Semiconductor Processing 40 (2015) 708-712.
[70] Awang A., Structural and Optical Properties of Erbium Doped Zinc Sodium Tellurite Glass: Effects of Gold Nanoparticles, PhD Thesis UTM (2014).
[71] Yusoff N.M., Sahar M.R., Effect of Silver Nanoparticles Incorporated with Samarium-Doped Magnesium Tellurite Glasses, Physica B 456 (2015) 191-196.
[72] Vincenzo A., Osman M.B., Francesco S., A Study of the Surface Plasmon Resonance of Silver Nanoparticles by the Discrete Dipole Approximation Method: Effect of Shape, Size, Structure and Assembly, Plasmonics 5 (2010) 85-97.
[73] Shekhar A., Soumyo M., Suparna M., Size-Controlled Silver Nanoparticles Synthesized over the Range 5-100 nm using the Same Protocol and Their Antibacterial Efficacy, The Royal Society of Chemistry 4 (2014) 3974-3983.
[74] Lodha G.S., Yamashita K., Kunieda H., Tawara Y., Yu J., Namba Y., Bennett J.M., Effect of Surface

Roughness and Subsurface Damage on Grazing Incidence X-Ray Scattering and Specular Reflectance, Applied Optics 37(22) (1998) 5239-5252.

[75] Fan M., Brolo A.G., Self-Assembled Au Nanoparticles as Substrates for Surface Enhanced Vibrational Spectroscopy: Optimization and Electrochemical Stability, Chemical Physics Chemistry 9 (2008) 1899-1907.

[76] Pantic M., Mitrovic S., Babic M., Jevremovic D., Kanjevac T., Dzunic D., Adamovic D., AFM Surface Roughness and Topography Analysis of Lithium Disilicate Glass Ceramic, Tribology in Industry 37(4) (2015) 391-399.

[77] Rao G.V., Shashikala H.D., Effect of heat treatment on optical, dielectric and mechanical properties of silver nanoparticle embedded $CaO\text{-}CaF_2\text{-}P_2O_5$ glass, Journal of Alloys and Compounds 622 (2015) 108-114.

[78] Pan Z., Ueda A., Aga Jr. R., Burger A., Mu R., Morgan S.H., Spectroscopic Studies of Er^{3+}Doped Ge-Ga-S Glass Containing Silver Nanoparticles, Journal of Non-Crystalline Solids 356 (2010) 1097-1101.

[79] Sobczyk M., Temperature Dependent Luminescence and Temperature Stimulated NIR to Vis Upconversion in Nd^{3+} doped $La_2O_3 – Na_2O – ZnO – TeO_2$ Glasses, Journal of Quantitative Spectroscopy & Radiative Transfer 119 (2013) 128-136.

[80] Ramakrishna P.V., Pammi S.V.N., Samatha K., UV-Visible Upconversion Studies of Nd^{3+} Ions in Tellurite Glass, Solid State Communications 155 (2013) 21-24.